Received: 20 May 2023, Accepted: 4 July 2023, Published: 29 December 2023 Publisher: UTP Press, Creative Commons: CC BY 4.0

UiO-67 MOF-BASED CATALYST AS A POTENTIAL PHOTOCATALYST FOR CO_2 CONVERSION TO METHANOL COMPLIMENTED BY RSM STUDIES

Moh Yuen Ying[1], Zulkifli Merican Aljunid Merican[1,2*], Abdurrashid Haruna[1,2,3], Suleiman Gani Musa[1,2,4]

[1]Department of Fundamental and Applied Sciences, Universiti Teknologi PETRONAS, Malaysia
[2]Institute of Contaminant Management, Universiti Teknologi PETRONAS, Malaysia
[3]Department of Chemistry, Ahmadu Bello University, Nigeria
[4]Department of Chemistry, Al-Qalam University Katsina, Katsina-Nigeria

*E-mail: zulkifli.aljunid@utp.edu.my

ABSTRACT

Metal-organic frameworks (MOFs) have received significant attention in recent years due to their fascinating properties, such as high surface area, porosity, tuneable pore size, and structural flexibility. These characteristics make them promising candidates for various applications, particularly in the photocatalytic conversion of carbon dioxide (CO_2). This research investigated the unitisation of Polyoxometalates (POMs) incorporated within MOFs as catalysts for converting CO_2 to methanol. The POM@MOF catalyst was prepared by the solvothermal method, and its physicochemical properties were characterised through various techniques, including FTIR, UV-VIS, PXRD, TGA, FESEM, and BET. Response Surface Methodology (RSM) based on Central Composite Design (CCD) was employed to optimise the reaction conditions, focusing on catalyst loading and reaction time. Methanol concentration in the product was determined using HPLC. Notably, the encapsulation of Keggin SW_{12} into UiO-67(Zr) resulted in better physicochemical properties than pristine UiO-67. The optimal reaction conditions were determined to be a catalyst loading of 1.0 g/L and a reaction time of 3 hours. While the photocatalytic CO_2 conversion was successfully conducted, methanol was not detected in both the proposed and modified experimental setups due to the low methanol concentration and the limitations of the detection instruments. This research establishes a lower-limit benchmark and contributes to the development of sustainable processes for CO_2 photocatalytic conversion to methanol utilising the SW_{12}@UiO-67 catalyst.

Keywords: *CO_2 conversion, Photocatalyst, RSM, UiO-67, POM@MOF*

INTRODUCTION

Carbon dioxide (CO_2), a significant greenhouse gas, is a major by-product of fossil fuel combustion. Massive CO_2 emissions have resulted in severe environmental problems such as global warming and extreme weather conditions. There has been a constant increase in atmospheric CO_2 levels, rising from approximately 280 ppm in the early 1800s to over 400 ppm in 2020 [1]. The Intergovernmental Panel on Climate Change (IPCC) forecasts that without significant mitigation measures, atmospheric CO_2 levels could exceed 950 ppm by 2100 [2]. Therefore, taking immediate action to reduce emissions and decrease atmospheric CO_2 levels is imperative.

As fossil fuels will continue to be a significant source of energy in the future, eliminating CO_2 from point sources is the most practical approach [3]. This can be accomplished through suitable carbon capture, storage, and utilisation (CCSU) techniques [4]-[5]. CCSU

includes capturing, transporting, and injecting carbon emissions deep underground into approved geological locations for long-term storage [6]-[7]. CO_2-enhanced oil recovery (CO_2-EOR) uses captured CO_2 directly for commercial activities. Implementing EOR in depleting oil fields not only provides well-defined locations for CO_2 storage but also generates additional oil as a source of income to cover the costs of CO_2 capture [7]-[8]. However, one major bottleneck of this technology is its energy consumption and non-renewable Nature, which may result in additional CO_2 emissions over time [1]. Another sustainable option involves capturing CO_2 and transforming it into high-value chemicals and fuels. However, the main limitation of CO_2 utilisation lies in the strong chemical stability of the C=O bond, which has a dissociation energy of more than 805 kJ mol^{-1} and requires relatively high energy for bond cleavage and CO_2 conversion [9].

In nature, the carbon cycle, essential for sustaining life on Earth, is maintained by green plants through photosynthesis. Researchers aspire to replicate the spontaneous conversion of atmospheric CO_2 and water into chemical fuels using sunlight as the only energy source. Solar energy, a renewable energy resource, can be used for the photochemical reduction of CO_2 by converting solar energy into chemical energy in the form of chemical bonds. A photocatalyst is required for the photochemical reduction of CO_2 to increase the efficiency and accelerate the reaction process. One of the pioneering works on solar energy conversion using photocatalysts was conducted by Fujishima in 1972, demonstrating UV-light-driven water splitting for hydrogen production employing TiO_2 [10]-[13]. Various materials have been developed for CO_2 capture and conversion applications, including ionic liquids, zeolites, porous carbons, and porous organic polymers [2],[14]. The major barrier to the conversion of carbon-containing resources is the existing low efficiency of photocatalysts toward CO_2 adsorption and conversion [15]. Therefore, the key to this technique lies in designing and synthesising high-performance photocatalysts with tuneable functionalities to overcome the limitations of current ones.

MOFs, a class of crystalline porous materials, have shown great potential for CO_2 capture and conversion due to their exceptional characteristics. These characteristics include a stable lattice, metal-containing active sites, tuneable pore size, high porosity, and a large surface area, which position MOFs as dominant players among other porous materials and semiconductors. This is evident in the accelerated increase in publications on MOFs over the years, showcasing their growing prominence in the field [15].

By strategically designing and functionalising the structure of MOFs, their physical and chemical properties can be adjusted, rendering them highly promising materials for a wide range of applications [16]-[17]. Zr-based MOFs are rapidly gaining prominence among all kinds of MOFs due to their thermal, chemical, and mechanical stabilities [18]. Zr-based MOFs can be effectively tailored for the photocatalytic conversion of CO_2. Among them, the UiO-series, including UiO-66, UiO-67, and UiO-68, have garnered significant attention in the field of MOFs since 2008. These UiO-series MOFs are known for their high stability, tuneability, porosity, and diverse functionalities, making them a rapidly expanding area of research in the field of MOFs [18].

UiOs' thermal stability has been demonstrated to reach temperatures of up to 500°C and remain stable in a variety of organic solvents [19]-[20]. UiO-66 has recently been utilised for CO_2 reduction. For example, introducing Cu into UiO-66-NH_2 could turn the CO_2 into liquid fuels. The conversion process yields methanol and ethanol, with conversion rates of 5.33 µmol and 4.22 µmol, respectively [19]. It has been discovered that UiO-66-NH_2 exhibits a maximum CO_2 uptake of 10.7 cm^3 g^{-1}, while O-ZnO demonstrates a maximum CO_2 uptake of 1.3 cm^3 g^{-1} at ambient temperature. This indicates that UiO-66 MOFs have a higher efficiency in adsorbing and removing CO_2 [21]. UiO-67, an analogue of the UiO-66, exhibits larger pores and a higher surface area due to the increase in the length of the linker, 4,4'-biphenyldicarboxylic acid (BPDC) instead of the terephthalic acid [22]-[23]. The comparison of UiO-66 and UiO-67 is shown in Table 1 [24].

Both CO and CO_2 are released as byproducts during fuel combustion processes with similar composition and bonding. Thus, it is worth noting and understanding specific chemical reactions or transformations that may occur in the study being discussed. For instance, the yield of reduction product C.O. from NH_2-UiO-66 is lower than that from NH2-UiO-67 since NH_2-UiO-67 can accommodate more guest CO_2 molecules by its longer functionalised linker [25]. The advanced study on UiO-67 is relatively new; thus, the current study is

expected to stimulate new perspectives in MOF-based photocatalysis for CO_2 reduction.

Table 1 Physical properties of UiO-66 and UiO-67

UiO's	BET surface area ($m^2\ g^{-1}$)	Pore size (nm)
UiO-66	1187	1.140
UiO-67	3000	2.114

The performance of the photocatalyst can be enhanced through techniques such as metal doping, ligand modification, and coupling with semiconductors [23],[26]-[27]. The challenges related to the tuneability, and stability of MOFs can be overcome by incorporating POMs as supporting materials, as demonstrated in recent studies [28]-[29]. When used as solid POM supports, MOFs have windows that allow the depositing of highly active POM materials. Both pristine MOF and POM stand to gain from creating the POM@MOF composite. This will increase catalytic activity while maintaining the necessary characteristics like porosity, stability, or substrate diffusion. In a wide range of heterogeneous catalytic processes, numerous examples of POM@MOF composites have been employed. In recent years, many photocatalytic uses of POM@MOF composites, including photocatalytic water splitting, CO_2 reduction and pollutant degradation [30]-[31].

Silicotungstic acid ($H_4W_{12}SiO_{40}$) is one of the well-known Keggin types of heteropoly acids (HPAs). HPAs have been pointed out lately as versatile, environmentally benign, water-stable, and green catalysts for a variety of organic reactions [32]. Based on the study done comparing SiW_{12}@CdMOF and PW_{12}@CdMOF, both exhibit high photocatalytic CO_2 reduction, but SiW_{12}@CdMOF has a higher C.O. yield of 4.35 mmol h^{-1} than PW_{12}@CdMOF of 3.60 mmol h^{-1} C.O. yield due to stronger electron-storage capacity in PW_{12} that reduces electron transfer between the framework and CO_2 molecules. In this work, silicotungstic acid is encapsulated into UiO-67 to improve the stability of UiO-67 and enhance the redox properties to assist in multi-electron and multi-proton transfer processes required for the conversion of CO_2.

MATERIALS AND METHODS

Materials and Reagents

All reagents used were of analytical grade and obtained from commercial suppliers. For the synthesis of UiO-67 MOF-based Catalysts, $H_4[SiW_{12}O_{40}]$ (>98%), N, N dimethylformamide (DMF) (>98%), benzoic acid (>98%), zirconium (IV) chloride (98%), [1,1'-biphenyl]-4,4'- dicarboxylic acid (BPDC) (98%), hydrochloric acid (37%), acetone (>99.8%) were obtained from Sigma Aldrich. Pure CO_2 gas and NaOH (98%) were used for the photocatalytic conversion experiment. All experimental work was conducted in a well-equipped fume hood, and distilled water was used throughout solution preparations. The materials used were listed down according to the step. All materials were used without any purification.

Catalyst Preparation

UiO-67 MOFs catalysts were synthesised and encapsulated through the solvothermal method, as shown in Figure 1 [33]. The solvothermal method involves the growth of single crystals from a non-aqueous solution inside a high-temperature autoclave. The solvothermal method allows for the customisation of crystal morphology, size, and pore size.

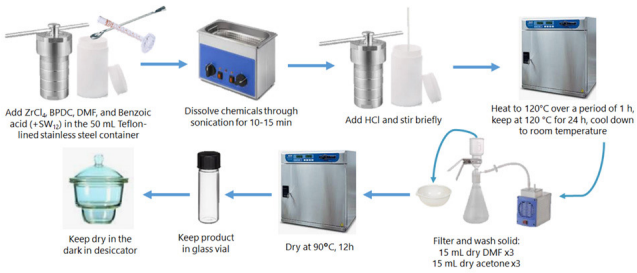

Figure 1 Schematic illustration of the preparation of UiO-67 and SW_{12}@UiO-67

Preparation of UiO-67

In a 50 mL vial, $ZrCl_4$ (116 mg, 0.5 mmol, 1 equivalent), BPDC (121 mg, 0.5 mmol, 1 equivalent), and benzoic acid (1.83 g, 15.0 mmol, 30 equivalent) were dissolved in 10 mL of DMF through 20 minutes of sonication at room temperature. 83 μL of 37% hydrochloric acid (fuming) was pipetted into the vial and sonicated for another 5 minutes. The mixture in the vial was then transferred to a 50 mL polytetrafluoro-ethylene-lined stainless-steel container and heated at 120°C for 24 hours in an oven (Memmert Universal Oven, 180L). After that, it was allowed to cool down to room temperature. The solid was filtered and washed with dry DMF (3 x 15 mL)

and dry acetone (3 x 15 mL) using a vacuum filtration unit, followed by drying at 90°C for 12 hours in the same oven. The final product was kept in the desiccator at 20 – 30% relative humidity.

Preparation of SW_{12}@UiO-67

In a 50 mL vial, $ZrCl_4$ (116 mg, 0.5 mmol, 1 equivalent), BPDC (121 mg, 0.5 mmol, 1 equivalent), $H_4[SiW_{12}O_{40}]$ (240 mg, 8.33×10^{-2} mmol, 1/6 equivalent) and benzoic acid (1.83 g, 15.0 mmol, 30 equivalent) were dissolved in 10 mL of DMF through 20 minutes of sonication at room temperature. 83 μL of 37% hydrochloric acid (fuming) was pipetted into the vial and sonicated for another 5 minutes. The mixture in the vial was then transferred to a 50 mL polytetrafluoroethylene-lined stainless-steel container and heated at 120°C for 24 hours in an oven. After that, it was allowed to cool down to room temperature. The solid was filtered and washed with dry DMF (3 x 15 mL) and dry acetone (3 x 15 mL) using a vacuum filtration unit, followed by drying at 90°C for 12 hours in the oven. The final product was kept in the desiccator at 20 – 30% relative humidity.

Characterisation

Six characterisation techniques, namely Fourier-transform Infrared Spectroscopy (FTIR), Ultraviolet-Visible Spectroscopy (UV-VIS), Powder X-ray Diffraction (PXRD), Thermal Gravimetric Analysis (TGA), Field Emission Scanning Electron Microscope (FESEM), and Surface Area and Porosity (SAP) analysis, were employed to analyse the UiO-67 MOF-based catalysts prepared using a solvothermal approach. FTIR (PerkinElmer Spectrum One as KBr pellets, scanning range of 4000 – 400 cm^{-1}) functioned to identify functional groups and chemical bonds in a molecule by generating an infrared spectrum of absorption. UV-VIS (Agilent brand, Cary100 model, scanning range of 100 – 700 nm) was conducted to determine the bandgap of the photocatalysts based on the absorbance spectra. The function of PXRD (Panalytical brand, Xpert3 Powder model, scanning range of 2 – 50°, exposure time of 1.2 s/step, step size of 0.01°/step) was to confirm phase identification of crystalline material of catalysts. The thermal stability of UiO-67 MOF-based catalysts was determined by TGA (Perkin Elmer brand, STA6000 model, heating range of 30 – 800°C, heating rate of 5°C/min). FESEM (Tescan brand, Clara model) was carried out to view the surface morphology of the catalysts at a magnification of 3 kX, 5 kX, 10 kX and 20 kX at an acceleration voltage of 10 keV. SAP analysis (Micromeritics brand, Tristar 3020 model, degassing temperature at 130°C) was used to confirm the surface area and pore size distribution of UiO-67 MOF-based catalysts through N_2 gas adsorption.

RSM Simulation Study

Response Surface Methodology (RSM) is a statistical technique to optimise the photocatalytic CO_2 conversion process and determine the best values for the independent variables. The experimental independent variables for this project are catalyst loading in g/L and reaction time in hours. These independent variables range selected were inserted into Design-Expert® software version 13 in RSM under the CCD model, and it would select the most suitable value or conditions for high methanol concentration, which was the dependent variable. The number of experiment runs with suitable parameters was identified, and the results obtained were analysed using CCD as well. Table 2 summarises the RSM parameters.

Table 2 Two parameters used in RSM

Parameters	Minimum value	Maximum value
Catalyst loading (g/L)	0.5	1.5
Reaction time (h)	1	5

Photocatalytic CO_2 Conversion to Methanol Experiment

The photocatalytic reactor setup is shown in Figure 2 [34]. The quartz photoreactor (2) was connected with a high-purity CO_2 inlet stream (1) (99.99%). The quartz photoreactor was filled with 100 mL of 0.1 M NaOH solution and 100 mg (1.0 g/L) of UiO-67 MOF-based catalysts. Pure CO_2 gas flowed into the airtight system for 30 minutes to eliminate dissolved oxygen and saturate the solution with CO_2 before irradiation by opening both V1 and V2 valves. After 30 minutes of equilibration in the dark, the quartz photoreactor was irradiated with a halogen lamp (150 W), mainly consisting of a visible light region. The intensity and wavelength of the light were 1379.67 W/m^2 and 400 – 750 nm, respectively. The light source was positioned 7 cm beside the photoreactor. During the photoreaction, the photoreactor was tightly closed, and the temperature of the photoreactor was maintained at 25 ± 1°C using a cooling fan. The stirring rate was set to 700 rpm. At the end of the reaction, the gas was released through

scrubber (3) containing H_2O for 3 minutes. 10 mL of liquid sample was then withdrawn using a syringe filter unit to remove the solid photocatalyst and placed in an airtight vial sealed with parafilm, where it was kept in an ice box at approximately 0°C until analysed by HPLC. The sample was monitored for methanol concentration using HPLC (Agilent brand with ICSep ICE-ORH-801 Column, 0.005M H_2SO_4 mobile phase, runtime 20 minutes, flowrate of 0.700 mL/min, column temperature of 65°C, RID temperature of 35°C). 2 mL of liquid sample was required, where only 50.0 µL of liquid sample was injected into the column [35]. Standard samples containing known concentrations of methanol (in the range of 5 – 150 ppm) were analysed to obtain a standard curve. The retention time of methanol was identified, and the calibration curve was established [36].

A blank reaction without any catalyst was carried out to ensure that the product formation was only due to the photocatalytic reduction of CO_2. In addition, an adsorption and desorption equilibrium to be reached in the dark, without irradiation with a pre-warmed lamp, is also required. These two simple precautions ensure the proper working for the photocatalyst loading under the optimal reaction rate [37]-[38].

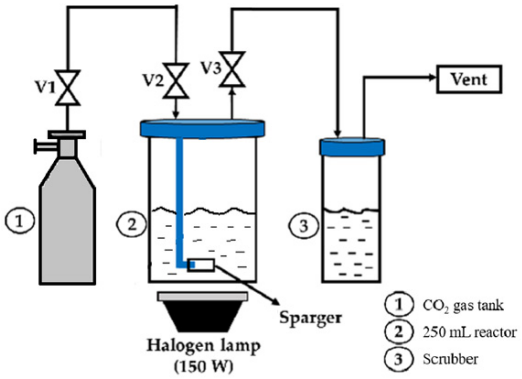

Figure 2 Photocatalytic equipment setup

RESULT AND DISCUSSION

Characterisation of SW_{12}@UiO-67 and UiO-67

FTIR, UV-VIS, TGA, PXRD, FESEM, and SAP analysis results for both SW_{12}@UiO-67 and UiO-67 were discussed in the subsequent sections.

Fourier-transform Infrared Spectroscopy (FTIR)

Figure 3 illustrates the FTIR spectra of SW_{12}@UiO-67 and UiO-67, with wavenumber ranging between 4000 – 400 cm^{-1}. From both spectra, vibrational bands at around 3412 cm^{-1}

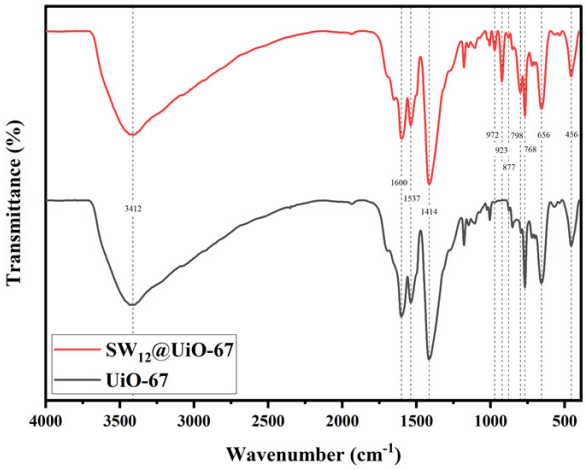

Figure 3 FTIR spectra of SW_{12}@UiO-67 and UiO-67

were due to hydroxyl stretching vibrations in the carboxylate group from the BPDC linker and the intercalated water. In contrast, the absorption peaks of 1600 cm^{-1} and 1537 cm^{-1} belonged to asymmetric stretching vibration of the carboxylate group from the BPDC linker. The absorption peaks at 768 cm^{-1}, 656 cm^{-1}, and 456 cm^{-1} indicate the Zr-O bonds in Zr nodes for UiO-67.

FTIR was used to confirm the encapsulation of silicotungstic acid into UiO-67. The intensity of UiO-67 absorption peaks in SW_{12}@UiO-67 remained the same and did not change after the encapsulation of silicotungstic acid. It can be proven by the fact that the peaks at 3412 cm^{-1}, 1600 cm^{-1}, 1537 cm^{-1}, 768 cm^{-1}, 656 cm^{-1}, and 456 cm^{-1} were all maintained with only an insignificant decrease in intensity. After the encapsulation of silicotungstic acid, several new peaks appeared in the FTIR spectrum of SW_{12}@UiO-67. The characteristic peak at 972 cm^{-1} was assigned to the asymmetric vibrations of the Si-O_a bond of SW_{12}. Apart from that, absorption peaks for silicotungstic acid at 923 cm^{-1}, 877 cm^{-1}, and 798 cm^{-1} attributed to W=O_d, W–O_b–W, and W–O_c–W asymmetrical vibrations in the SW_{12} structure [39]. Through the FTIR spectrum, it can be observed that the SW_{12} structure was successfully incorporated in the UiO-67 pores and windows without changing the original UiO-67 MOFs structure.

Ultraviolet-Visible Spectroscopy (UV-VIS)

The UV-Vis absorption spectra of the catalysts are shown in Figure 4. Both UiO-67 and SW_{12}@UiO-67 show an absorption peak at around 350 nm, gradually

increasing in the visible light range (380–700 nm). The sudden jump in absorption observed around 350 nm in Figure 4 can be attributed to a specific phenomenon known as ligand-to-metal charge transfer (LMCT) in UiO-67 [40]. The absorption of light at 350 nm indicates that UiO-67 can also absorb light in the U.V. range. The encapsulation of silicotungstic acid in UiO-67 results in a stronger light absorption than pristine UiO-67, as shown in the UV-Vis spectra in Figure 4, where the spectrum of SW_{12}@UiO-67 is plotted at a higher value than the spectrum of UiO-67. A higher absorbance signifies increased light absorption, leading to a higher likelihood of electronic transition. SW_{12} has higher absorbance as it assists multi-electron and multi-proton transfer processes due to the presence of multiple metal centres.

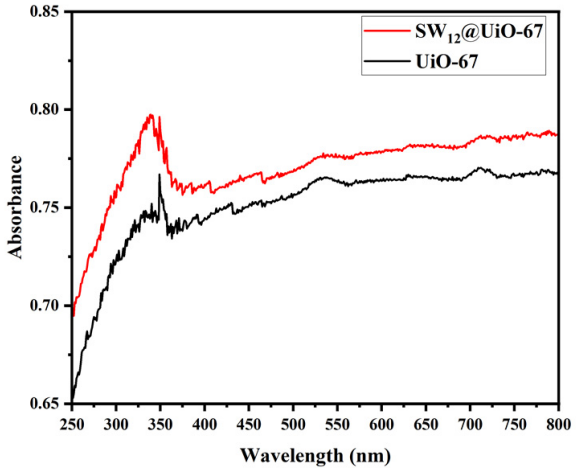

Figure 4 UV-VIS spectra of SW_{12}@UiO-67 and UiO-67

Thermal Gravimetric Analysis (TGA)

The thermogravimetric plots of both SW_{12}@UiO-67 and UiO-67 are shown in Figure 5. UiO-67 showed an initial weight loss at the temperature range of 30 – 100°C, evidently owing to the loss of guest molecules held in the catalyst during synthesis, which could be water molecules, organic ligands, and other volatile materials [41]. The initial weight loss could be observed in SW_{12}@UiO-67 as well, but the mass change decreased gradually with temperature. Lower initial weight loss of SW_{12}@UiO-67 was attributed to the encapsulation of SW_{12}, which had a smaller pore size and volume than pristine UiO-67, and fewer guest molecules were trapped in the framework structure [42]. The smaller pore size and volume could be evidently shown in the SAP results. The second weight loss was noticeable at the temperature range of 500 – 600°C, where the weight percentage decreased sharply from around 80% to 55% for pristine UiO-67 and 85% to 60% for SW_{12}@UiO-67. This second weight loss was attributed to the decomposition of the framework. The weight losses for both materials occur at the same temperature at 575°C, indicating that the thermal stability of the framework was not affected by the encapsulation of SW_{12}. The remaining weight for UiO-67 and SW_{12}@UiO-67 were 48.3 wt% and 55.8 wt%, respectively. The higher weight percentage of SW_{12}@UiO-67 compared to UiO-67 is due to the presence of significant amount of silicotungstic compound encapsulated within the porous structure of UiO-67. Thus, the TGA results further confirmed that the encapsulation of SW_{12} in the UiO-67 was done and would not influence its framework thermal stability [43].

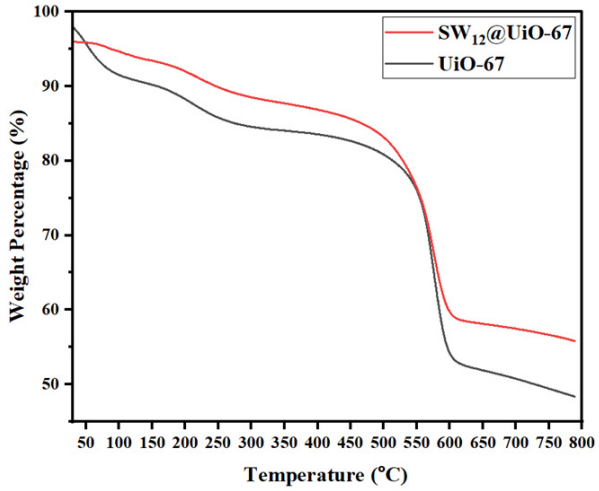

Figure 5 Thermogravimetric plots of SW_{12}@UiO-67 and UiO-67

Powder X-ray Diffraction (PXRD)

The crystalline structures and phase composition of UiO-67 and SW_{12}@UiO-67 were characterised by PXRD, as shown in Figure 6. The diffraction peak at $2\theta = 6.1°$ was identified in the crystalline structure of the UiO-67, while the diffraction peaks for SW_{12}@UiO-67 were observed at $2\theta = 5.7°$ and 6.5°. The strong intensity of peaks at $2\theta = 5.7°$ and 6.5° corresponds to peaks of 111 and 200 crystal surface, proving the formation of the crystalline phase of UiO-67 [44]. When SW_{12} was encapsulated into the UiO-67 structure, the main diffraction peaks were not changed compared to that of the pristine UiO-67, but the intensity of the diffraction peaks was increased due to the higher scattering power of SW_{12} compared to Zr. The diffraction peaks of both UiO-67 and SW_{12}@UiO-67 matched well and had a good agreement with the other reported UiO-67 works, which indicates that the introduction of SW_{12} would not affect the structure of UiO-67.

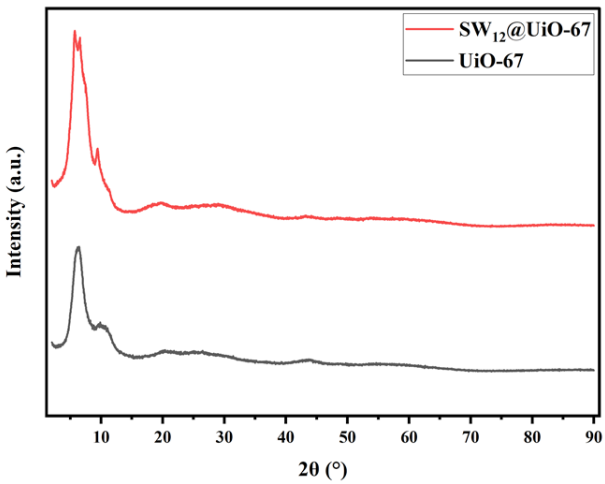

Figure 6 Diffractogram pattern of SW_{12}@UiO-67 and UiO-67

Field Emission Scanning Electron Microscope (FESEM)

The morphologies of the UiO-67 and SW_{12}@UiO-67 were observed by FESEM, as shown in Figures 7 and 8. Based on Figure 7, the framework of UiO-67 was observed to have a prominent octahedral shape. The individual octahedral crystals formed due to the addition of benzoic acid as a modulator during the synthesis [44]. Crystal growth can be observed in Figure 8, where the octahedral shape of UiO-67 was still visible, but the layering growth of SW_{12} made the framework less well-defined. As SW_{12} was encapsulated in the cages of UiO-67 to form crystalline materials POM@MOF, the structure should remain an octahedral shape. The irregular shape of SW_{12}@UiO-67 might be due to the addition of excess SW_{12} amount during synthesis, which causes the crystal size to vary between 5 μm–300 nm [42]. The crystal size of UiO-67 was measured to be in the range of 3 – 5μm.

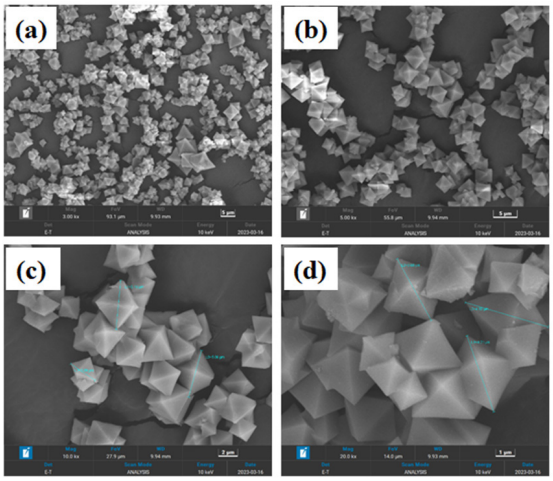

Figure 7 FESEM images of UiO-67 at a magnification of (a) 3 kX, (b) 5 kX, (c) 10 kX, and (d) 20 kX

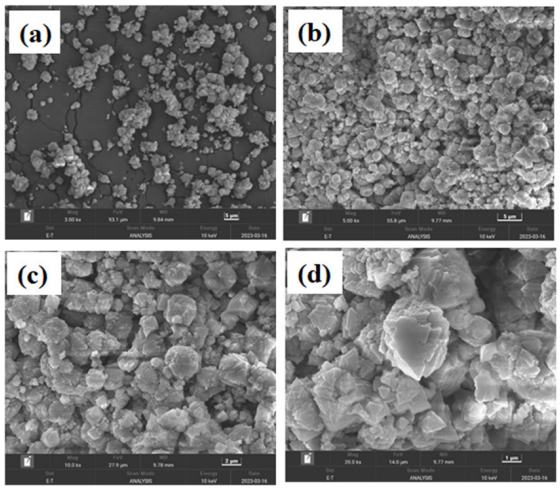

Figure 8 FESEM images of SW_{12}@UiO-67 at a magnification of (a) 3 kX, (b) 5 kX, (c) 10 kX, and (d) 20 kX

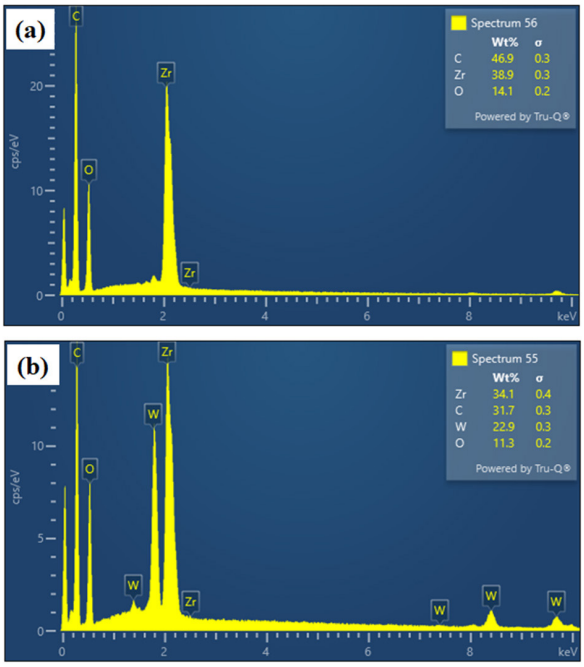

Figure 9 EDX spectra of (a) UiO-67 and (b) SW_{12}@UiO-67

The SW_{12}@UiO-67 and UiO-67 were further analysed using Energy Dispersive X-ray (EDX) Microanalysis to determine the chemical composition of the respective catalysts. EDX has emerged as the most employed surface-analysis method because all elements can be determined from the binding energies of photoelectrons released during X-ray excitation, except for hydrogen and helium. Hydrogen and helium both have no core electrons available to be removed for X-ray emission. The EDX results for both catalysts are shown in Figure 9. UiO-67 with the chemical formula

of $C_{84}H_{52}O_{32}Zr_6$ was detected to have 46.9% of C, 38.9% of Zr, and 14.1% of O. SW_{12}@UiO-67 with the chemical formula of $H_4[SiW_{12}O_{40}]@C_{84}H_{52}O_{32}Zr_6$ was detected to have 34.1% of Zr, 31.7% of C, 22.9% of W, and 11.3% of O. EDX is a centre point analysis, where the point of analysis might have an insignificant amount of Si because they are embedded inside the framework, so Si was not detected in the EDX. Further analysis with advanced instruments such as X-ray Photoelectron Spectroscopy (XPS) can be done to detect Si.

Surface Area and Porosity (SAP) Analysis

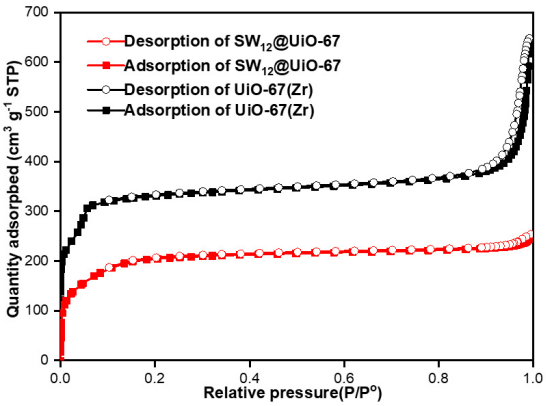

Figure 10 Nitrogen adsorption and desorption isotherms of SW_{12}@UiO-67 and UiO-67

Figure 10 shows the nitrogen adsorption and desorption isotherms of SW_{12}@UiO-67 and UiO-67. Both isotherms are similar to type IV according to IUPAC classification, indicating the mesoporous texture of the samples. The Brunauer-Emmett-Teller (BET) surface areas and pore size were calculated from N2 adsorption data; BET surface area of UiO-67 is 1117 $m^2 g^{-1}$ while for SW_{12}@UiO-67 is 705 $m^2 g^{-1}$. BET surface area of the UiO-67 was reported to be 2180 $m^2 g^{-1}$ [45]. The BET surface area of synthesised UiO-67 was lower than the reported value, which might be due to the unavoidable error in controlling the reaction conditions during synthesis. A high BET surface area is advantageous in carbon capture applications. SW_{12}@UiO-67 possessed a smaller surface area than UiO-67 due to the presence of SW_{12}, where SW_{12} partially blocked the pores in UiO-67. As a result, it gave SW_{12}@UiO-67 a lower porosity and surface area [45]. The pore size of UiO-67 was 9.13582 nm, while the pore size of SW_{12}@UiO-67 was 6.23803 nm. It is consistent with the TGA result, where the encapsulation of SW_{12} into the UiO-67 cage will reduce the pore size.

Response Surface Methodology

RSM is a statistical tool used to represent the relationship between independent variables and dependent variables. In this work, process optimisation was carried out using the standard design of RSM through CCD, where it was employed to represent the relationship between significant operating parameters and the methanol concentration in ppm. The significant operating parameters were catalyst loading in g/L and reaction time in hours. As shown in the following sections, the optimised reaction conditions for photocatalytic CO_2 conversion to methanol were at 1.0 g/L catalyst loading and 3-hour reaction time. It was estimated that 5.6 ppm of methanol could be obtained when using these reaction conditions.

Data Analysis using RSM

The 13 runs using the CCD model based on the input parameters of catalyst loading (0.5 g/L – 1.5 g/L) as A and reaction time (1 h – 5 h) as B were listed in Table 3. The methanol concentration from CO_2 conversion determined by previous findings was used for the generation of data [1],[19],[46]-[48]. According to the CCD model, each numeric factor was set to five levels: plus, and minus.

Standard	Run	Factor 1 A: Catalyst loading (g/L)	Factor 2 B: Reaction time (h)	Response 1 Methanol concentration (ppm)
3	1	0.5	5	3.3
2	2	1.5	1	2.1
4	3	1.5	5	5.9
1	4	0.5	1	0.4
11	5	1.0	3	5.0
10	6	1.0	3	5.3
6	7	2.0	3	5.8
13	8	1.0	3	5.2
8	9	1.0	6	6.3
5	10	0.3	3	1.5
7	11	1.0	0.5	0.5
12	12	1.0	3	5.4

Table 3 RSM estimation for 2 parameters resulting in 13 runs using CCD model

Alpha (axial points), plus and minus 1 (factorial points) and the centre point. The five levels for A were 2.0 g/L

and 0.3 g/L (axial points), 1.5 g/L and 0.5 g/L (factorial points), and 1.0 g/L (centre point). Whereas the five levels for B were 6 h and 0.5 h (axial points), 5 h and 1 h (factorial points), and 3 h (centre point). The 13 runs were composed of 5 centre points and eight non-centre points. The actual methanol concentration (ppm) based on computed 13 runs was compared with the predicted result from the software, as shown in Figure 11.

The post-ANOVA statistics in Table 4 show the R^2 value of 0.9825, which indicates a good fit for the model. R^2 was determined to check the accuracy of the predicted value with the experimental value, where the value near one indicates a good fit. The Predicted R^2 of 0.8854 was in reasonable agreement with the Adjusted R^2 of 0.9701, where the difference was less than 0.2. The signal-to-noise ratio was measured through adequate precision, where a ratio greater than four is desirable. The ratio of this model was 26.509, indicating an adequate signal. In addition, the model showed a low standard deviation of 0.1651, implying that the data were clustered closely around the mean value of 1.11. This model was reliable and could be used to navigate the design space.

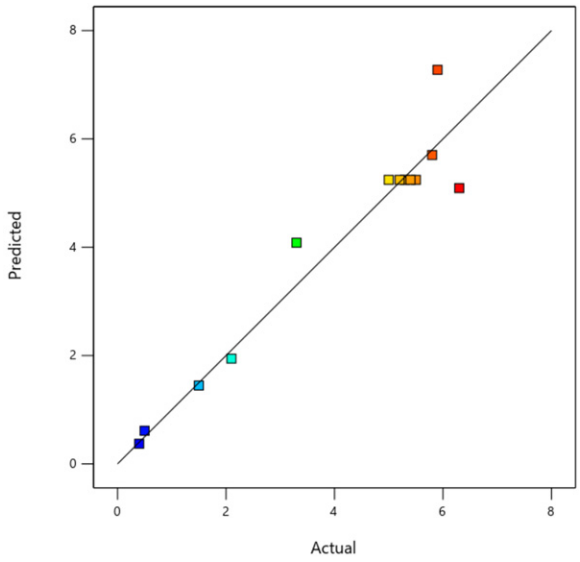

Figure 11 Predicted vs actual methanol concentration (ppm) based on computed 13 runs

Table 4 Post-ANOVA fit statistic

Std. Dev.	0.1651	R^2	0.9825
		Adjusted R^2	0.9701
Mean	1.11	Predicted R^2	0.8854
C.V. %	14.89	Adeq Precision	26.5094

Dimensional Response Surface Graph

Figure 12 depicts the 3-dimensional response surface model graph with mesh colour. Red indicates the highest methanol concentration, while blue indicates the lowest methanol concentration.

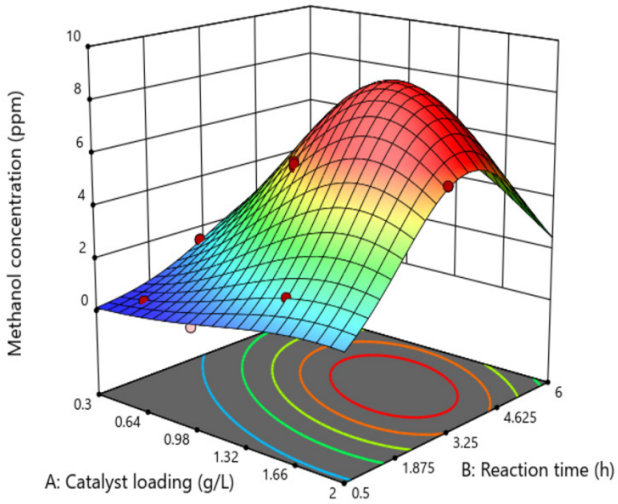

Figure 12 3-Dimensional response surface model graph of methanol concentration with catalyst loading and reaction time

The colour changes according to the independent variables. The horizontal plane of the figure represents the area of variation of two factors, and the vertical axis materialises the variation of the response from the model [49]. The z-axis was the methanol concentration (ppm), while the x-axis and y-axis were catalyst loading and reaction time, respectively. This response surface model graph shows the relationship between the catalyst loading and reaction time to achieve a high methanol concentration. Based on the graph, a low catalyst loading at 0.3 g/L and a short reaction time of 0.5 h would result in low methanol concentration, which is nearly 0 ppm in the blue colour area. The optimal setting to achieve a high methanol concentration of around 8 ppm appears to be at the red colour area with a catalyst loading range of 1.0 – 2.0 g/L and reaction time range of 3.25 – 4.625 h. At the reaction time of 0.5 h, the response surface colour changes from blue to light blue when the catalyst loading increases from 0.3 g/L to 2.0 g/L, indicating that an increase in catalyst loading will increase the methanol concentration. It should be noted that a high catalyst loading could scatter the incident radiations and hinder proper illumination of the entire reaction volume, which might decrease the concentration of methanol produced [50]. On the other hand, the longer the reaction time, the

higher the methanol concentration, but the methanol concentration decreases after a certain reaction time. This drop in methanol concentration after a long reaction time might be due to the formation of HCOOH from generated methanol [51]. The contour graph in Figure 13 gives a simpler view of the influence of two factors on the methanol concentration. This concluded the parameters used for the experimental procedure with a condition of catalyst loading of 1.0 g/L and reaction time of 3 h, which is estimated to give rise to around 6 ppm of methanol concentration.

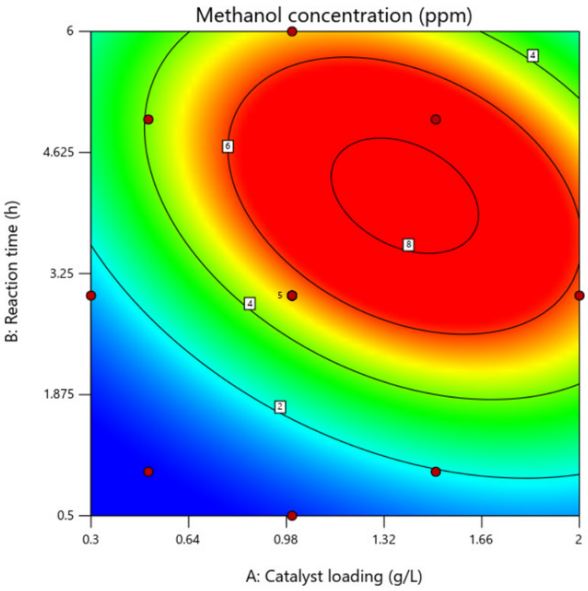

Figure 13 Contour graph of methanol concentration with catalyst loading and reaction time

Photocatalytic CO_2 Conversion to Methanol

The solvent used was 0.1M NaOH solution. Alkaline solvent allowed a higher solubility of CO_2, which could enhance the methanol production rate. The dissolved CO_2 within an alkaline solvent would generate carbonates and bicarbonates. The reaction equations of both ions to methanol were shown in Equations 2 and 3 [52].

$$H_2CO_3 + 6H^+ + 6e^- \rightarrow CH_3OH + 2H_2O \quad (2)$$

$$CO_3^{2-} + 8H^+ + 6e^- \rightarrow CH_3OH + 2H_2O \quad (3)$$

Both SW_{12}@UiO-67 and UiO-67 were used in the photocatalytic reaction to convert CO_2 to methanol. The photocatalytic reaction for both photocatalysts was carried out under the conditions of 1.0 g/L catalyst loading and 3 h reaction time. Five standards of methanol and distilled water mixture with known concentrations of 5 ppm, 10 ppm, and 100 ppm served as an external standard for the HPLC analysis. The chromatogram of HPLC analysis for 100 ppm of methanol in water, 10 ppm of methanol in water, 5 ppm of methanol in water, a liquid sample of photocatalytic reaction using UiO-67, and a liquid sample of photocatalytic reaction using SW_{12}@UiO-67 were depicted in Figures 14 –18.

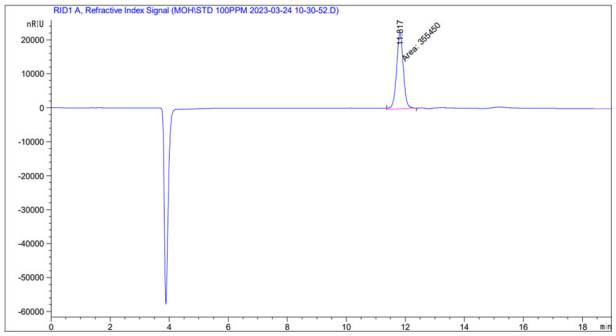

Figure 14 Chromatogram of HPLC for 100 ppm of methanol in water

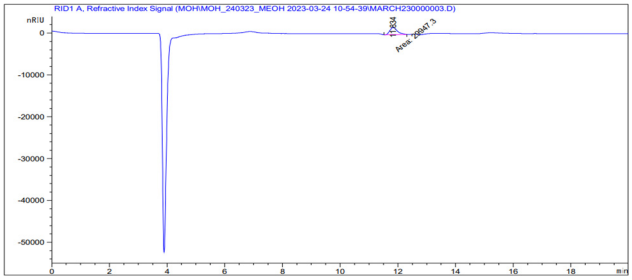

Figure 15 Chromatogram of HPLC for 10 ppm of methanol in water

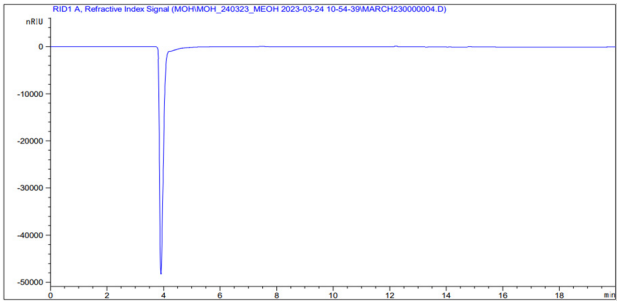

Figure 16 Chromatogram of HPLC for 5 ppm of methanol in water

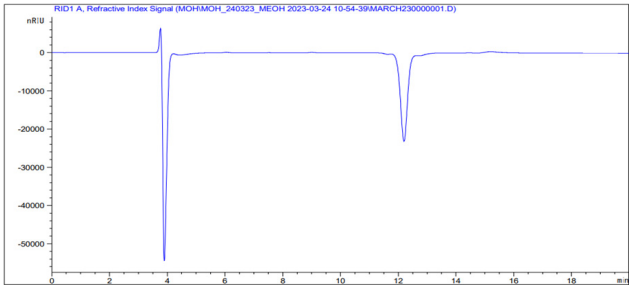

Figure 17 Chromatogram of HPLC for a liquid sample of photocatalytic reaction using UiO-67

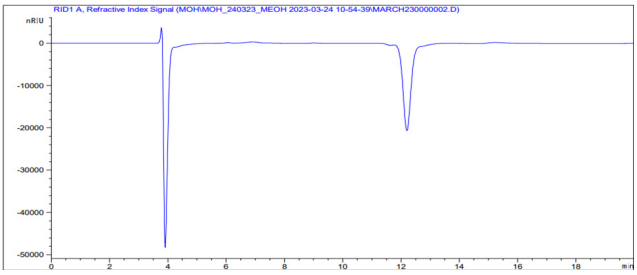

Figure 18 Chromatogram of HPLC for a liquid sample of photocatalytic reaction using SW_{12}@UiO-67

Based on the chromatograms for methanol standards in Figures 14 and 15, the methanol peak was at the retention time of 11.8 min. The negative peak in the chromatogram at nearly 4.0 min indicated the presence of water. In Figure 15, the methanol peak for 10 ppm was visibly small, while the methanol peak for 5 ppm in Figure 16 was almost unnoticeable. For the rerun, both liquid samples from the photocatalytic reaction using UiO-67 and SW_{12}@UiO-67 did not peak at 11.8 min in the chromatograms from Figures 17 and 18. The negative peak in both liquid sample chromatograms at around 12.1 min was unidentified, which was possible to be a compound produced from the reaction. Therefore, the result for methanol concentration was not obtained.

The detection limit of the HPLC instrument was the confounding factor for the detection of methanol. Figure 16 shows that no peak was observed in the chromatogram with 5 ppm of methanol. The expected methanol concentration to be detected under the reaction conditions of 1.0 g/L catalyst loading and 3 h reaction time was 5.6 ppm. A methanol concentration lower than 5.6 ppm was anticipated as the experimental yield would be lower than the computed yield. Thus, methanol might be present in the liquid samples, but it could not be detected due to the low sensitivity of the HPLC instrument. Besides, it was possible to have no methanol production at all, where the kinetic drawback made methanol formation more difficult than carbon monoxide and formic acid because more electrons are required for methanol formation. The interaction between photocatalyst and adsorbed CO_2 might undergo one-electron reactions instead of a multi-electron reaction [53]. Thus, other products were formed instead of methanol, and it was then not detected.

To provide better recommendations for further study, it is suggested to reevaluate and revise the experimental parameters based on a more comprehensive literature review. This could involve expanding the range of catalyst loading and adjusting the reaction time accordingly. The effect of other reaction parameters, such as type of catalysts, light intensity, and temperature, on the photocatalytic CO_2 conversion to methanol can be studied in future work. More sensitive and accurate detection methods can also be developed for low-concentration methanol liquid products.

CONCLUSION

In conclusion, POMs incorporated within MOFs as photocatalysts for CO_2 conversion to methanol have shown great potential. Both SW_{12}@UiO-67 and UiO-67 were successfully prepared by the solvothermal method. The synthesised SW_{12}@UiO-67 composite exhibited better physicochemical properties compared to the pristine UiO-67, as evidenced by the characterisation results of FTIR, UV-VIS, PXRD, TGA, FESEM, and SAP analyses. The optimised reaction conditions for photocatalytic CO_2 conversion to methanol were 1.0 g/L catalyst loading and 3-hour reaction time using CCD of RSM. However, despite the successful conduct of the photocatalytic CO_2 conversion reaction, methanol was not detected in both proposed and modified experimental setups due to low methanol concentration and low instrument detection limit, which were identified as the main confounding factors.

This project contributes to understanding the challenges in developing sustainable processes for CO_2 photocatalytic conversion to methanol. SW_{12}@UiO-67 is undeniably a novel photocatalyst with a high potential for CO_2 conversion to methanol, providing a promising area for future research. Further studies can be conducted to enhance the performance of the catalyst and develop more accurate detection methods for low-concentration methanol products. Overall, this project highlights the importance of continued research efforts in developing sustainable energy sources and reducing greenhouse gas emissions.

ACKNOWLEDGMENTS

The authors would like to appreciate Universiti Teknologi PETRONAS and the Yayasan UTP grant funding (YUTP-FRG 1/2022/015LC0-458). We acknowledge the UTP

Centralized Analytical Laboratory (CAL), CO_2 Research Centre (CO_2RES) and Institute of Contaminant Management, Universiti Teknologi PETRONAS, for all the support.

REFERENCES

[1] I. I. Alkhatib, C. Garlisi, M. Pagliaro, K. Al-Ali, and G. Palmisano, "Metal-Organic Frameworks for Photocatalytic CO_2 Reduction Under Visible Radiation: A Review of Strategies and Applications," *Catalysis Today*, vol. 340, pp. 209-224, 2020, doi: 10.1016/j.cattod.2018.09.032.

[2] M. Ding, R. W. Flaig, H. -L. Jiang, and O. M. Yaghi, "Carbon Capture and Conversion Using Metal-Organic Frameworks and MOF-Based Materials," *Chemical Society Reviews*, vol. 48, no. 10, pp. 2783-2828, 2019, doi: 0.1039/c8cs00829a.

[3] A. Haruna, G. Tanimu, I. Ibrahim, Z. N. Garba, S. M. Yahaya, S. G. Musa, and Z. M. A. Merican, "Mitigating Oil and Gas Pollutants for a Sustainable Environment – Critical Review and Prospects," *Journal of Cleaner Production*, vol. 416, p. 137863, 2023, doi: 10.1016/j.jclepro.2023.137863.

[4] F. D. Lauro, C. Tregambi, F. Montagnaro, P. Salatino, R. Chirone, and R. Solimene, "Improving the Performance of Calcium Looping for Solar Thermochemical Energy Storage and CO_2 Capture," *Fuel*, vol. 298, p. 120791, 2021, doi: 10.1016/j.fuel.2021.120791.

[5] S. Tripathi, S. Choudhary, A. Meena, and K. M. Poluri, "Carbon Capture, Storage, and Usage With Microalgae: A Review," *Environmental Chemistry Letters*, vol. 21, pp. 2085–2128, 2023, doi: 10.1007/s10311-023-01609-y

[6] V. Núñez-López and E. Moskal, "Potential of CO_2-EOR for Near-Term Decarbonization," *Frontiers in Climate,* vol. 1, no. 5, 2019, doi: 10.3389/fclim.2019.00005.

[7] K. O. Yoro and M. O. Daramola, "CO_2 Emission Sources, Greenhouse Gases, and the Global Warming Effect," *Advances in Carbon Capture Methods, Technologies and Applications*, pp. 3-28, 2020, doi: 10.1016/B978-0-12-819657-1.00001-3.

[8] M. L. Godec, V. A. Kuuskraa, and P. Dipietro, "Opportunities for Using Anthropogenic CO_2 for Enhanced Oil Recovery and CO_2 Storage," *Energy & Fuels,* vol. 27, no. 8, pp. 4183-4189, 2013, doi: 10.1021/ef302040u.

[9] H. Wang, " Nanostructure@Metal-Organic Frameworks (MOFs) For Catalytic Carbon Dioxide (CO_2) Conversion in Photocatalysis, Electrocatalysis, and Thermal Catalysis ," *Nano Research*, vol. 15, pp. 2834-2854, 2022, doi: 10.1007/s12274-021-3984-9.

[10] A. Fujishima and K. Honda, "Electrochemical Photolysis of Water at a Semiconductor Electrode," *Nature*, vol. 238, no. 5358, pp. 37-38, 1972, doi: 10.1038/238037a0.

[11] A. Haruna, I. Abdulkadir, and S. O. Idris, "Synthesis, Characterization and Photocatalytic Properties of $Bi0.85{-}XMXBa0.15FeO_3$ (M = Na and K, X = 0, 0.1) Perovskite-Like Nanoparticles Using the Sol-Gel Method," *bmn* vol. 32, no. 1, pp. 896-903, 2020, doi: 10.1016/j.jksus.2019.05.005.

[12] A. Haruna, I. Abdulkadir, and S. O. Idris, "Photocatalytic Activity and Doping Effects of $BiFeO_3$ Nanoparticles in Model Organic Dyes," *Heliyon*, vol. 6, no. 1, 2020, doi: 10.1016/j.heliyon.2020.e03237.

[13] A. Haruna, F. K. Chong, Y. C. Ho, and Z. M. A. Merican, " Preparation and Modification Methods of Defective Titanium Dioxide-Based Nanoparticles for Photocatalytic Wastewater Treatment—a Comprehensive Review," *Environmental Science and Pollution Research*, vol. 29, no. 47, pp. 70706-70745, 2022, doi: 10.1007/s11356-022-22749-8.

[14] S. G. Musa, Z. M. A. Merican, and A. Haruna, "Investigation of Isotherms and Isosteric Heat of Adsorption for PW11@HKUST-1 composite," *Journal of Solid State Chemistry*, vol. 314, p. 123363, 2022, doi: 10.1016/j.jssc.2022.123363.

[15] Y. Ma, Z. Wang, X. Xu, and J. Wang, "Review on Porous Nanomaterials for Adsorption and Photocatalytic Conversion of CO_2," *Chinese Journal of Catalysis*, vol. 38, no. 12, pp. 1956-1969, 2017, doi: 10.1016/S1872-2067(17)62955-3

[16] A. Haruna, Z. M. A. Merican, S. G. Musa, and S. Abubakar, "Sulfur Removal Technologies From Fuel Oil for Safe and Sustainable Environment," *Fuel*, vol. 329, p. 125370, 2022, doi: 10.1016/j.fuel.2022.125370.

[17] A. Haruna, Z. M. A. Merican, and S .G. Musa, "Recent Advances in Catalytic Oxidative Desulfurization of Fuel Oil – A review," *Journal of Industrial and Engineering Chemistry*, vol. 112, pp. 20-36, 2022, doi: 10.1016/j.jiec.2022.05.023.

[18] A. H. Vahabi, F. Norouzi, E. Sheibani, and M. Rahimi-Nasrabadi, "Functionalized Zr-UiO-67 Metal-Organic Frameworks: Structural Landscape and Application," *Coordination Chemistry Reviews*, vol. 445, p. 214050, 2021, doi: 10.1016/j.ccr.2021.214050

[19] Q. Du, R. Rao, F. Bi, …N. Liu, and X. Zhang, "Preparation of Modified Zirconium-Based Metal-Organic Frameworks (Zr-MOFs) Supported Metals and Recent Application in Environment: A review and Perspectives," *Surfaces and Interfaces*, vol. 28, 2022, doi: 10.1016/j.surfin.2021.101647

[20] X. -Q. Zhan, F. -C. Tsai, L. Xie, …D. Shi, and T. Jiang, "Ligands-Coordinated Zr-Based MOF for Wastewater Treatment," *Nanomaterials*, vol. 8, no. 9, p. 655, 2018, doi: 10.3390/nano8090655.

[21] J. Meng, Q. Chen, J. Lu, and H. Liu, "Z-Scheme Photocatalytic CO_2 Reduction on a Heterostructure of Oxygen-Defective ZnO/Reduced Graphene Oxide/UiO-66-NH_2 under Visible Light," *ACS Applied Materials & Interfaces*, vol. 11, no. 1, pp. 550–562, 2019, doi: 10.1021/acsami.8b14282.

[22] H. Ali-Moussa, R. N. Amador, J. Martinez, F. Lamaty, M. Carboni, and X. Bantreil, "Synthesis and Post-synthetic Modification of UiO-67 Type Metal-Organic Frameworks by Mechanochemistry," *Materials Letters*, vol. 197, pp. 171–174, 2017, doi: 10.1016/j.matlet.2017.03.140

[23] M. S. Ramyashree, S. S. Priya, N. C. Freudenberg, K. Sudhakar, and M. Tahir, "Metal-Organic Framework-Based Photocatalysts for Carbon Dioxide Reduction to Methanol: A Review on Progress and Application," *Journal of CO_2 Utilization*, vol. 43, 2021, doi: 10.1016/j.jcou.2020.101374.

[24] S. Yuan, L. Feng, K. Wang, …J. Li, and H. C. Zhou, "Stable Metal–Organic Frameworks: Design, Synthesis, and Applications," *Advanced Materials*, vol. 30, no. 37, p. 1704303, 2018, doi: 10.1002/adma.201704303.

[25] F. Guo, Y. -P. Wei, S. -Q. Wang, X. -Y. Zhang, F. -M. Wang, and W. -Y. Sun, "Pt Nanoparticles Embedded in Flowerlike NH_2-UiO-68 for Enhanced Photocatalytic Carbon Dioxide Reduction," *Journal of Materials Chemistry A*, vol. 7, no. 46, pp. 26490–26495, 2019, doi: 10.1039/c9ta10575a.

[26] A. Haruna, I. Abdulkadir, and S. O. Idris, "Effect of Annealing Temperature on the Synthesis and Photocatalytic Properties of $Bi0.65K0.2Ba0.15FeO_3$ Perovskite-Like Nanoparticle Synthesized by Sol-Gel Method," *Beni-Suef University Journal of Basic and Applied Sciences*, vol. 9, no. 8, pp. 1-8, 2020, doi: 10.1186/s43088-020-0033-9.

[27] A. Haruna, I. Abdulkadir, and S. O. Idris, "Visible Light Induced Photodegradation of Methylene Blue in Sodium Doped Bismuth Barium Ferrite Nanoparticle Synthesized by Sol-gel Method," *Avicenna Journal of Environmental Health Engineering*, vol. 5, no. 2, pp. 120-126, 2018, doi: 10.15171/ajehe.2018.16.

[28] A. Haruna, Z. M. A. Merican, and S. G. Musa, "Remarkable Stability and Catalytic Performance of $PW_{11}M$@MOF-808 (M=Mn and Cu) Nanocomposites for Oxidative Desulfurization of Fuel oil," *Molecular Catalysis*, vol. 541, p. 113079, 2023, doi: 10.1016/j.mcat.2023.113079.

[29] A. Haruna, Z. M. A. Merican, S. G. Musa, and M. B. A. Rahman, "MOF-808(Zr)-Supported With Keggin Polyoxometalates as an Efficient Oxidative Desulfurization Catalyst," *Journal of the Taiwan Institute Chemical Engineers*, vol. 147, p. 104919, 2023, doi: 10.1016/j.jtice.2023.104919

[30] Y. Liu, C. Tang, M. Cheng, …Y. Fu, and L. Li, "Polyoxometalate@Metal–Organic Framework Composites as Effective Photocatalysts," *ACS Catalalysis*, vol. 11, no. 21, pp. 13374-13396, 2021, doi: 10.1021/acscatal.1c03866.

[31] Y. -P. Wei, Y. Liu, F. Guo, X. -Y. Dao, and W. -Y. Sun, "Different Functional Group Modified Zirconium Frameworks for the Photocatalytic Reduction of Carbon dioxide," *Dalton Transactions*, vol. 48, no. 23, pp. 8221-8226, 2019, doi: 10.1039/c9dt01767d.

[32] K. Nikoofar, "Silicotungstic Acid ($H_4SiW_{12}O_{40}$): An Efficient Keggin Heteropoly Acid Catalyst for the Synthesis of Oxindole Derivatives," *Arabian Journal of Chemistry*, vol. 10, no. 2, pp. 283-287, 2017, doi: 10.1016/j.arabjc.2014.07.008.

[33] W. Salomon, C. Roch-Marchal, P. Mialane, …L. Ruhlmann, and A. Dolbecq, "Immobilization of Polyoxometalates in the Zr-Based Metal Organic Framework UiO-67," *Chemical Communications*. vol. 51, pp. 2972-2975, 2015, doi: 10.1039/c4cc09986a.

[34] N. T. Sahrin, R. Nawaz, C. F. Kait, S. L. Lee, and M. D. H. Wirzal, "Visible Light Photodegradation of Formaldehyde Over TiO_2 Nanotubes Synthesized via Electrochemical Anodization of Titanium Foil," *Nanomaterials*, vol. 10, no. 1, p. 128, 2020, doi: 10.3390/nano10010128.

[35] C. -C. Kuo, Y. -H. Wen, C. -M. Huang, H. -L. Wu, and S. -S. Wu, "A Removable Derivatization HPLC for Analysis of Methanol in Chinese Liquor Medicine," *Journal of Food and Drug Analysis*, vol. 10, no. 2, pp. 101-106, 2002, doi: 10.38212/2224-6614.2757.

[36] D. J. Boston, Y. M. F. Pachón, R. O. Lezna, N. R. D. Tacconi, and F. M. MacDonnell, 2014. "Electrocatalytic and Photocatalytic Conversion of CO_2 to Methanol Using Ruthenium Complexes with Internal Pyridyl Cocatalysts," *Inorganic Chemistry*, vol. 53, no. 13, pp. 6544-6553, 2014, doi: 10.1021/ic500051m.

[37] M. A. Hoque and M. I. Guzman, "Photocatalytic Activity: Experimental Features to Report in Heterogeneous Photocatalysis," *Materials*, vol. 11, no. 10, 2018, doi: 10.3390/ma11101990.

[38] S. Singh, A. Modak, and K. K. Pant, "CO_2 Reduction to Methanol Using a Conjugated Organic–Inorganic Hybrid TiO2–C3N4 Nano-assembly," *Transactions of the Indian National Academy of Engineering*, vol. 6, pp. 395-404, 2021, doi: 10.1007/s41403-021-00201-6.

[39] C. Zhang, Z. Zheng, K. Liu, M. Debliquy, and Q. Liu, "Highly Sensitive and Selective Sb2WO6 Microspheres in Detecting VOC Biomarkers in Cooked Rice: Experimental and Density Functional Theory Study," *Food Chemistry*, vol. 424, p. 136323, 2023, doi: 10.1016/j.foodchem.2023.136323.

[40] S. Govindaraju, P. Puthiaraj, M. H. Lee, and K. Yun, "Photoluminescent AuNCs@UiO-66 for Ultrasensitive Detection of Mercury in Water Samples," *ACS Omega,* vol. 3, no. 9, pp. 12052-12059, 2018, doi: 10.1021/acsomega.8b01665.

[41] P. Kumar, A. Kumar, B. Sreedhar, B. Sain, S. S. Ray, and S. L. Jain, "Cobalt Phthalocyanine Immobilized on Graphene Oxide: An Efficient Visible-Active Catalyst for the Photoreduction of Carbon Dioxide," *Chemistry – A European Journal*, vol. 20, no. 20, pp. 6154-6161, 2014, doi: 10.1002/chem.201304189.

[42] X. Dong, Y. Lin, Y. Ma, and L. Zhao, "Ce-Doped UiO-67 Nanocrystals With Improved Adsorption Property for Removal of Organic Dyes," *RSC Advances*, vol. 9, pp. 27674-27683, 2019, doi: 10.1039/c9ra05586j.

[43] F. Yan, Q. Wang, F. Wang, and Z. Huang, "Study on Energy Storage Properties of Metal-Organic Frameworks Nanofluids (UiO-67/Water and UIO-67/Methanol) By an Experimental and Theoretical Method," *Journal of Materials Science*, vol. 56, pp. 10008-10017, 2021, doi: 10.1007/s10853-021-05910-5.

[44] R. Vakili, S. Xu, N. Al-Janabi, P. Gorgojo, S. M. Holmes, and X. Fan, "Microwave-Assisted Synthesis of Zirconium-Based Metal-Organic Frameworks (MOFs): Optimization and Gas Adsorption," *Microporous and Mesoporous Materials*, vol. 260, pp. 45-53, 2018, doi: 10.1016/j.micromeso.2017.10.028.

[45] W. Zhao, C. Zhang, Z. Yan, … L. Jiang, and F. Li, "Preparation, Characterization, and Performance Evaluation of UiO-66 Analogues as Stationary Phase in HPLC for the Separation of Substituted Benzenes and Polycyclic Aromatic Hydrocarbons," *PLoS One*, vol. 12, no. 6, 2017, p. e0178513, doi: 10.1371/journal.pone.0178513.

[46] R. Guil-López, N. Mota, N. J. Llorente, …J. L. G. Fierro, and R. M. Navarro, "Methanol Synthesis from CO_2: A Review of the Latest Developments in Heterogeneous Catalysis, " *Materials*, vol. 12, no. 23, p. 3902, 2019. doi: 10.3390/ma12233902.

[47] E. S. Gutterød, A. Lazzarini, T. Fjermestad, …A. Nova, and U. Olsbye, "Hydrogenation of CO_2 to Methanol by Pt Nanoparticles Encapsulated in UiO-67: Deciphering the Role of the Metal-Organic Framework," *Journal of the American Chemical Society*, vol. 142, no. 2, pp. 999–1009, 2020, doi: 10.1021/jacs.9b10873.

[48] A. Lais, M. A. Gondal, M. A. Dastageer, and F. F. Al-Adel, "Experimental Parameters Affecting the Photocatalytic Reduction Performance of CO_2 to Methanol: A Review," *International Journal of Energy Research*, vol. 42, no. 6, pp. 2031-2049, 2018, doi: 10.1002/er.3965.

[49] G. Bouazza, M. Assou, E. H. Chatri, and S. Souabi, "Optimization by the Response Surface Methodology of Color," in *1st International Conference on Innovative Research in Applied Science, Engineering and Technology (IRASET)*, 2020, pp. 1-5, doi: 10.1109/IRASET48871.2020.9092012.

[50] R. K. De_Richter, T. Ming, and S. Caillol, "Fighting Global Warming by Photocatalytic Reduction of CO_2 Using Giant Photocatalytic Reactors," *Renewable and Sustainable Energy Reviews,* vol. 19, pp. 82-106, 2013, doi: 10.1016/j.rser.2012.10.026.

[51] D. Kumar, A. Lee, T. Lee, M. Lim, and D. K. Lim, "Ultrafast and Efficient Transport of Hot Plasmonic Electrons by Graphene for Pt Free, Highly Efficient

Visible-Light Responsive Photocatalyst," *Nano Letters*, vol. 16, no. 3, pp. 1760-1767, 2016, doi: 10.1021/acs.nanolett.5b04764.

[52] H. Abdullah, M. R. Khan, M. Pudukudy, Z. Yaakob, and N. A. Ismail, "CeO_2-TiO_2 as a Visible Light Active Catalyst for the Photoreduction of CO_2 to Methanol," *Journal of Rare Earths*, vol. 33, no. 11, pp. 1155-1161, 2015, doi: 10.1016/S1002-0721(14)60540-8.

[53] K. Li, X. An, K. H. Park, M. Khraisheh, and J. Tang, "A critical Review of CO_2 Photoconversion: Catalysts and Reactors," *Catalysis Today*, vol. 224, pp. 3-12, 2014, doi: 10.1016/j.cattod.2013.12.006.